



Heriot-Watt University
Research Gateway

Partial dissolution of carbonate rock grains during reactive CO₂-saturated brine injection under reservoir conditions

Citation for published version:

Singh, K, Anabaraonye, BU, Blunt, MJ & Crawshaw, J 2018, 'Partial dissolution of carbonate rock grains during reactive CO₂-saturated brine injection under reservoir conditions', *Advances in Water Resources*, vol. 122, pp. 27-36. <https://doi.org/10.1016/j.advwatres.2018.09.005>

Digital Object Identifier (DOI):

[10.1016/j.advwatres.2018.09.005](https://doi.org/10.1016/j.advwatres.2018.09.005)

Link:

[Link to publication record in Heriot-Watt Research Portal](#)

Document Version:

Publisher's PDF, also known as Version of record

Published In:

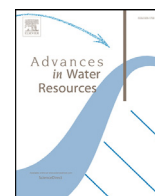
Advances in Water Resources

General rights

Copyright for the publications made accessible via Heriot-Watt Research Portal is retained by the author(s) and / or other copyright owners and it is a condition of accessing these publications that users recognise and abide by the legal requirements associated with these rights.

Take down policy

Heriot-Watt University has made every reasonable effort to ensure that the content in Heriot-Watt Research Portal complies with UK legislation. If you believe that the public display of this file breaches copyright please contact open.access@hw.ac.uk providing details, and we will remove access to the work immediately and investigate your claim.



Partial dissolution of carbonate rock grains during reactive CO₂-saturated brine injection under reservoir conditions

Kamaljit Singh^{a,*}, Benaiah U. Anabaraonye^b, Martin J. Blunt^a, John Crawshaw^b

^a Qatar Carbonates and Carbon Storage Research Centre, Department of Earth Science and Engineering, Imperial College London, SW7 2AZ London, UK

^b Qatar Carbonates and Carbon Storage Research Centre, Department of Chemical Engineering, Imperial College London, SW7 2AZ London, UK



ARTICLE INFO

Keywords:

Reactive transport
Ghost features
Carbonate rocks
Carbon capture and storage (CCS)
X-ray micro-tomography
FIB-SEM

ABSTRACT

One of the major concerns of carbon capture and storage (CCS) projects is the prediction of the long-term storage security of injected CO₂. When injected underground in saline aquifers or depleted oil and gas fields, CO₂ mixes with the resident brine to form carbonic acid. The carbonic acid can react with the host carbonate rock, and alter the rock structure and flow properties. In this study, we have used X-ray micro-tomography and focused ion beam scanning electron microscopy (FIB-SEM) techniques to investigate the dissolution behavior in wettability-altered carbonate rocks at the nm- to μm-scale, to investigate CO₂ storage in depleted oil fields that have oil-wet or mixed-wet conditions. Our novel procedure of injecting oil after reactive transport has revealed previously unidentified (ghost) regions of partially-dissolved rock grains that were difficult to identify in X-ray tomographic images after dissolution from single fluid phase experiments. We show that these ghost regions have a significantly higher porosity and pore sizes that are an order of magnitude larger than that of unreacted grains. The average thickness of the ghost regions as well as the overall rock dissolution decreases with increasing distance from the injection point. During dissolution micro-porous rock retains much of its original fabric. This suggests that considering the solid part of these ghost regions as macro (bulk) pore space can result in the overestimation of porosity and permeability predicted from segmented X-ray tomographic images, or indeed from reactive transport models that assume a uniform, sharp reaction front at the grain surface.

1. Introduction

Carbon capture and storage (CCS) is one of the proposed methods to mitigate climate change. For CCS, carbon dioxide (CO₂) can be captured from various industrial units, such as power plants, cement factories, and iron and steel making industries (Boot-Handford et al., 2014). The captured CO₂ is pressurized and transported to a storage site, and then injected underground for its geological storage in saline aquifers, depleted oil and gas reservoirs, or deep coal seams. There are four mechanisms by which the CO₂ can be stored underground: physical trapping under an impermeable cap rock; trapping of CO₂ due to its dissolution in the brine phase, where CO₂-rich brine sinks due to its higher density; capillary trapping where the CO₂ is stored as isolated trapped clusters; and mineral trapping in which the CO₂ can react with the host rock to form secondary carbonates (Xu et al., 2003; Krevor et al., 2015; Bachu et al., 1994).

A major challenge of CCS is the long-term security of stored CO₂ (Herzog et al., 2003). During CO₂ injection, when the supercritical CO₂ mixes with the resident brine, it forms carbonic acid. The carbonic acid can react with the host rock and consequently can alter the rock

structure, pore geometry and related flow properties such as absolute and relative permeability (Qajar and Arns, 2017; Menke et al., 2015; Luquot and Gouze, 2009; Luquot et al., 2014; Ott and Oedai, 2015). This is particularly the case for carbonate rocks. The extent and pattern of rock dissolution depend on many factors including pH, temperature-pressure conditions, injection rates, pore structure, and chemical and physical heterogeneity (El-Maghraby et al., 2012; Menke et al., 2017; Al-Khulaifi et al., 2018; Daccord et al., 1993). Recently, it has been shown that the dissolution pattern is also different for single-phase and two-phase reactive transport (Ott and Oedai, 2015). The latter involves the simultaneous injection of CO₂ and reactive brine. These studies demonstrate the complexity of reactive transport and dissolution processes. Understanding the mechanisms of these processes is therefore important to estimate the fluid flow, pore occupancy and the effectiveness of CCS projects.

Recent advances in three-dimensional imaging using X-ray tomography have enabled the visualization and characterization of porous media at different length scales (Krevor et al., 2015; Ott and Oedai, 2015; Singh et al., 2017a,b; Singh et al., 2016; Pak et al., 2015; Berg et al., 2013; Blunt et al., 2013; Blunt, 2017). Medical X-ray tomography

* Corresponding author.

E-mail address: kamaljit.singh@imperial.ac.uk (K. Singh).

has been applied to investigate mm- to dm-scale features of reactive transport and dissolution regimes in rocks with varying degrees of heterogeneity (Ott and Oedai, 2015; Menke et al., 2018). To investigate reactive transport at the pore scale, X-ray micro-tomography has been used in recent experimental studies (Qajar and Arns, 2017; Menke et al., 2015, 2017; Al-Khulaifi et al., 2018; Ott et al., 2012; Qajar and Arns, 2016). However, the finer features of rock dissolution, from the nm- to μm -scale, have not been studied in detail. The visualization of these features and their effect on flow properties are important to understand the overall behavior of carbonate rock dissolution.

In this study, we have used X-ray micro-tomography and FIB-SEM techniques to investigate the dissolution features of wettability-altered carbonate rocks, at different length scales, after supercritical CO_2 -saturated reactive brine injection. The wettability of these rocks was altered by the adsorption of organic acids (Hamouda and Rezaei Gomari, 2006) to represent the surface properties of rocks expected in hydrocarbon reservoirs. Injecting oil after reactive transport has revealed previously unidentified (ghost) features of partially-dissolved rock grains. We characterize these ghost features at the nano-scale using FIB-SEM. The detection of the ghost features has important implications for predicting single- and two-phase flow behavior, especially for carbonate rocks that almost ubiquitously have intra-grain micro-porosity (Cantrell et al., 2004).

2. Experimental methods

2.1. Materials

The experiments were conducted on a 3.8 mm diameter and 13.3 mm long Ketton limestone rock sample from the Ketton quarry, Rutland, UK, which contains >99% calcite (Andrew et al., 2014). The Ketton rock contains both inter-grain macro-porosity and intra-grain micro-porosity (Tanino and Blunt, 2012). The cored sample was first cleaned with methanol using a Soxhlet extraction apparatus for 24 h, followed by drying in a vacuum oven at 100 °C for 24 h.

A solution of 5 wt% sodium chloride (NaCl) salt (Sigma-Aldrich, UK) in deionized water was used as the aqueous phase. The reactive fluid used in this study was a pre-equilibrated solution of supercritical CO_2 and 5 wt% NaCl brine, which was equilibrated in a Hastelloy Parr reactor equipped with a stirrer, at a pressure of 10 MPa and temperature of 50 °C for at least 24 h. A 50 wt% mixture of decane (Sigma-Aldrich, UK) and iododecane (Sigma-Aldrich, UK), was selected as the oil. The decane was doped with iododecane to obtain an effective X-ray micro-tomography contrast with brine and rock.

2.2. Pre-treatment of the rock sample

The wettability of macro pores in the cleaned Ketton sample (initially strongly water-wet) was altered to oil-wet, whereas the micro (intra-grain) pores remained water-wet as they did not contact oil directly. This wettability state represents the surface properties of carbonate rocks expected in hydrocarbon reservoirs or depleted oil fields. To achieve this, the sample was placed in a cylindrical Viton sleeve that was attached to metal end pieces on both sides allowing fluid to be pumped through the rock. A water-wet nylon membrane (Whatman®, UK) with a pore diameter of 0.2 μm was placed at the base of the sample. The water-wet membrane was used to restrict the passage of oil (non-wetting phase) during oil injection from the top of the sample, therefore establishing a maximum oil saturation in the macro pore space, while the intra-grain micro pores remained water-saturated. The metal end pieces were fitted to PEEK tubing. The sample assembly was loaded in a Hassler type flow cell made of carbon fiber which is nearly transparent to X-rays. A confining pressure of 2 MPa was applied to confine the Viton sleeve to avoid fluid bypassing along the walls of the sample.

The sample was flushed with CO_2 at a flow rate of 0.5 mL/min for approximately 30 min to displace air. This was followed by injecting

deionized (DI) water at 0.2 mL/min for 30 min to remove both gaseous and dissolved CO_2 in water, ensuring 100% water saturation. A 0.01 M solution of stearic acid in decane (hereafter refer to as *doped-oil*) was injected from the top of the sample at a flow rate of 0.01 mL/min until the oil phase invaded the pores of the nylon filter. The breakthrough of the doped-oil was determined by pressure monitoring. The flow rate was then increased to 0.1 mL/min. The use of a water-wet nylon membrane and high flow rate ensured that the water was displaced completely from the macro pore space by doped-oil. The system was left for 24 h at ambient conditions for ageing to alter the wettability of the oil-filled pore space. The change in the wettability occurs due to the attraction of the negatively charged tail of stearic acid in doped-oil to the positively charged calcium ions, forming a layer of calcium stearate that offers strongly oil-wet conditions (Hamouda and Rezaei Gomari, 2006; Hansen et al., 2000). Note that the wettability alteration occurred only in the macro pore space of the sample, and the smaller intra-grain micro-pores that have much smaller diameter (Tanino and Blunt, 2012) than that of pores of the nylon filter remained water-wet. This was also confirmed by conducting an additional experiment in which the water was doped with potassium iodide (7 wt%) to obtain an effective X-ray absorption contrast with oil (decane) in the pore space, see Fig. S1 (Supplementary Information) for details.

The sample was then flushed with DI water from the base of the sample at a flow rate 0.1 mL/min for more than 200 pore volumes, to ensure maximum removal of the doped-oil phase. The sample was then unloaded from the core holder and the sleeve, and left in the vacuum oven at 100 °C for 24 h for drying.

2.3. Experimental and X-ray micro-tomographic imaging protocol

The wettability-altered dry rock sample was loaded in the core holder, using the same procedure as explained in the previous section. The rock sample was imaged before fluid injection (dry scans) with a voxel size of 2 μm and 5 μm , using a Zeiss Xradia 500 Versa X-ray micro-tomography scanner with 80 kV and 7 W settings. The sample was first scanned at a lower resolution with a voxel size of 5 μm at multiple locations along the height of the sample. These scans were then stitched together to obtain a total height of ~ 10.3 mm, the center of which was at ~ 6.54 mm from the base of the 13.3 mm long rock sample. The total size of the complete image was $1020 \times 1079 \times 2055$ voxels. For each tomographic image, we acquired a total number of 2200–2800 projections. Two high resolution images, with a voxel size of 2 μm , were acquired near the top and the base of the sample at a distance of ~ 9.5 mm and ~ 3.5 mm from the base of the sample respectively. A total of 4000 projections were acquired for each high resolution tomographic image.

2.3.1. Brine saturation and pressurizing the system

The sample was saturated with brine using the same procedure as used during the pre-treatment of the rock sample. The pressure in the brine and the confining fluid (DI water) was then raised to 10 MPa and 12 MPa respectively. A higher pressure was used to confine the Viton sleeve, in which the sample was mounted, to avoid any fluid bypassing along the walls of the sample. The temperature of the system was raised to 50 °C.

2.3.2. Reactive flow

The reactive fluid (pre-equilibrated supercritical CO_2 -saturated brine) was then injected from the base (inlet) of the sample at a flow rate of 0.1 mL/min for 168 min 10 s. The reactive brine was then completely replaced with a non-reactive brine at a flow rate of 0.1 mL/min for 24 min. We acquired two images (near inlet and outlet) at a voxel size of 2 μm ; however the scan near the inlet was discarded because of the image artefacts created by sample shift during stage rotation and scanning.

2.3.3. Oil and brine injection

After reaction, oil (50 wt% mixture of decane and iododecane) was injected from the top (outlet) of the brine-saturated sample at a flow rate 0.015 mL/min to 0.1 mL/min, followed by brine injection from the base (inlet) of the sample at a flow rate of 0.015 mL/min. The sample was scanned at a voxel size of 5 μm at multiple locations along the height of the sample. These scans were then stitched together to obtain a complete image of the sample. Two high resolution images, with a voxel size of 2 μm , were acquired near the top and the base of the sample at same locations as for the dry scans.

2.3.4. Image processing and analysis

The tomograms were reconstructed using proprietary software provided by Zeiss and processed using Avizo-9 software unless otherwise specified. The tomograms were pre-processed to remove distorted outer regions.

The stitched image (5 μm voxel size) of the dry rock sample was filtered using a non-local means edge preserving filter (Fig. S2a, Supplementary Information). This was then segmented into two phases (solid and pore space) using a seeded watershed algorithm based on the gray-scale gradient and gray-scale intensity of each voxel.

The images (5 μm voxel size) after dissolution followed by sequential oil and brine flooding were used for the evaluation of dissolution at the larger (cm) scale. As the brine-filled pore space was not clearly distinguishable due to the presence of partially dissolved regions that have similar gray scale to that of brine, we used three intensity thresholds for segmenting the brine-filled pore space. In Seg A (Fig. S2b), the brine-filled pore space represented by the darkest color in Fig. S2a was assigned as brine, while in Seg B (Fig. S2c), a part of the partially dissolved regions (intermediate gray in Fig. S2a) was also assigned as brine. In Seg C (Fig. S2d), all the dark and intermediate gray regions were considered as brine. In a subsequent step, the oil (white) was segmented and merged with the segmented brine to obtain the complete pore space. The pore space from the segmented dry scan was also merged to assure that the pore space is completely captured. The segmentation thresholds were used to investigate the effect of selecting different segmentation thresholds on the overall porosity profiles and permeability.

Due to intermediate gradient and intensity values, some of the voxels adjacent to oil were segmented as rock phase (Fig. S3, Supplementary Information). To correct for this artefact, we used a sequential erosion and dilation of the grain phase by 2 voxels with 26 neighborhood. This procedure removed the unwanted oil layer while keeping the rest of the image unchanged (Fig. S3). The corrected image was used for post-processing.

The porosity of a given slice j of the segmented images was obtained as:

$$\phi_j = \text{class}_0 / (\text{class}_0 + \text{class}_1) \quad (1)$$

where class_0 and class_1 represent the number of pixels attributed to the pore and solid phase in a given slice respectively.

2.3.5. Simulations for permeability and flow fields

For the flow simulations, we used an open source CFD software, OpenFOAM (Muljadi et al., 2016). First, the pore space was isolated from the segmented images. The flow through the isolated pores was computed by solving the incompressible Navier–Stokes equation as:

$$\rho \left(\frac{\partial u}{\partial t} + u \cdot \nabla u \right) = -\nabla p + \mu \nabla^2 u \quad (2)$$

$$\nabla \cdot u = 0 \quad (3)$$

$$u = 0 \text{ at grain boundaries}$$

where u is the velocity vector, and p is the pressure. Here, a boundary condition of constant pressure drop between the inlet and the outlet of the image was used, and a no-slip boundary condition was used on the

solid walls. The simulations were run until a steady-state solution of the equation ($\partial u / \partial t = 0$) was achieved. These computations resulted in pressure and velocity fields as well as the permeability of the samples (Bijeljic et al., 2013). The values of the velocity fields were corrected for the Darcy velocity used in the experiments.

2.3.6. Estimation of thickness/width of partially dissolved regions

The thickness (width) of partially dissolved regions of rock grains after reactive flow was estimated from high-resolution tomographic images (voxel size of 2 μm) acquired after sequential oil and brine injection. Fig. S4 (Supplementary Information) shows an example image containing rock, brine, oil and partially dissolved regions. Here, the dark intermediate gray-scale represents the partially dissolved regions of rock grains, indicated by the red arrow. As the interface (boundary) between brine (in the pore space) and the partially dissolved regions is diffused, it was difficult to measure the exact thickness of partially dissolved regions from segmented images obtained after dissolution. However, the injected oil (white) allowed the identification of the boundary of the bulk pore space (occupied by oil) and the partially dissolved regions unambiguously. We then visually identified the boundary between partially dissolved regions and the unreacted part of the grain. This boundary is marked by the dashed-yellow line in Fig S4. The thickness of partially dissolved regions was then measured manually between these two boundaries. This is shown as 't' between two blue arrows indicating two boundaries. Using the same procedure, we measured thickness at more than 400 locations for each high-resolution image (one near the inlet and the other near the outlet of the sample).

2.4. SEM and FIB-SEM

2.4.1. Sample preparation

The sample after sequential oil and brine flooding was flushed with DI water from the base at a flow rate of 0.3 mL/min for 10 min. It was then cleaned by sequential injection of toluene (for 11 min), methanol (for 11 min) and DI water (for 15 min) at a flow rate of 0.3 mL/min. The sample was then dried in a vacuum oven at 100 $^{\circ}\text{C}$ for 24 h.

The dried sample was embedded in a fluorensite epoxy resin at a pressure of 4 MPa following the procedure of Shah et al. (2014). At this pressure, the epoxy occupied the complete pore space in the rock sample including the micro-porous regions. The sample was then cut and polished using a polycrystalline diamond abrasive suspension to expose an internal plane for subsequent SEM and FIB-SEM analysis. The polished sample was scanned in three dimensions using a Heliscan microCT scanner (Thermo Fisher Scientific) at a voxel size of 4.65 μm .

2.4.2. Scanning

The FIB-SEM was conducted using an FEI Quanta 3D DualBeam FIB-SEM scanner in the Electron Microscopy Suite of the Cavendish Laboratory at the University of Cambridge (UK). A 1 μm thick platinum layer was deposited on a 15 \times 15 μm area around the region of interest, which helped to enhance the image contrast. Trenches were excavated around the selected location from three sides, which helped to reduce shadowing effects.

Two locations were selected for FIB-SEM, one where the rock was undissolved after reactive brine injection (control location – A1), and the other where the rock was partially dissolved (A2). The location A2 was selected at a distance of \sim 20–27 μm from the bulk pore space. We acquired a series of 8-bit two-dimensional SEM images (after sequential cutting using a focused ion beam) that were stacked together to obtain a complete three-dimensional image. For the locations A1 and A2, a voxel size of 14.1 \times 17.7 \times 25.4 nm and 13.7 \times 17.1 \times 25.2 nm (in X, Y and Z directions) was obtained respectively. For these images, we used the backscattered imaging mode of the FIB-SEM to negate charging effects.

As the field of view for FIB-SEM is limited (approximately 10–18 μm), we also excavated two long trenches at different locations to

visualize the entire partially dissolved region near grain boundaries using SEM. The location A3 was selected near location A2 (approximately 43 μm away). The location A4 was selected at a distance of approximately 1.9 mm from A3, toward the inlet of the sample. The SEM scans were acquired with a pixel size of 53.9 nm and 111.5 nm at locations A3 and A4 respectively. The details of these locations are provided in Section 3.

2.4.3. Image processing

For the SEM and FIB-SEM images, we applied a machine learning Weka segmentation approach (Arganda-Carreras et al., 2017) using ImageJ software. This segmentation approach is extremely useful for segmenting images with low signal-to-noise ratio. For this work, we applied this technique on 8-bit filtered FIB-SEM images and unfiltered SEM images.

The pore space of the segmented FIB-SEM images was isolated, which was then separated into individual pores and throats using a maximal ball algorithm (Dong and Blunt, 2009; Raeni et al., 2017). The radius of each pore was obtained by calculating the radius of the maximum inscribed sphere in that pore.

2.4.4. Energy-dispersive X-ray spectroscopy (EDX) analysis

We also performed EDX analysis to identify different phases in the FIB-SEM images. Fig. S5a (Supplementary Information) shows two locations (S1 and S2) where the EDX maps were generated. Fig. S5b shows the energy spectra at these two locations. A clear peak of calcium (Ca) at location S1 confirms the light-gray regions in the SEM image as the rock phase.

2.5. Dimensionless numbers

The Péclet number (Pe), the ratio of advective to diffusive transport flux, is defined as:

$$Pe = U_{av} L / D \quad (4)$$

where U_{av} (m/s) is the average pore interstitial velocity (ratio of the Darcy velocity to the scanned porosity measured from the segmented dry scan), L (m) is the characteristic length and D is the molecular diffusion coefficient of Ca^{2+} in water at 25 °C ($7.5 \times 10^{-10} \text{ m}^2/\text{s}$) (Menke et al., 2015, 2017). The scanned porosity ($\phi_s = 0.1457$) of the rock sample is considered in these calculations as the bulk flow is focused in large macro pores that are captured in the segmented dry scan. The characteristic length was estimated from $L = \pi/S$ (Menke et al., 2015), where S is the specific surface area ($S = A_S/V_B$). Here, A_S is the surface area (m^2) that was computed from the segmented image, and V_B is the bulk (total) volume of the scanned sample.

The Damköhler number Da , the ratio of reaction rate to advective transport rate, is defined as:

$$Da = \pi r / (U_{av} n) \quad (5)$$

where the number of moles of calcite per unit volume of rock, $n = \rho_{calcite} [1 - \phi_{total}] / M_{calcite}$, $\rho_{calcite}$ is the density of pure calcite ($2.71 \times 10^3 \text{ kg/m}^3$), ϕ_{total} is the total porosity measured using helium pycnometry ($\phi_{total} = 0.2337$) (Andrew et al., 2014), and $M_{calcite}$ is the molecular mass of calcite (0.1 kg/mol). The surface reaction rate of pure calcite ($r = 8.1 \times 10^{-4} \text{ mol/m}^2/\text{s}$ at 50 °C and 10 MPa (Peng et al., 2015)) is based on the combination of two parallel reactions:



The calculated Péclet number and Damköhler number are 789 and 1.21×10^{-4} respectively. For these calculations, we used $U_{av} = 1.01 \times 10^{-3} \text{ m/s}$ and $S = 5.352 \times 10^3 \text{ m}^{-1}$. A high value of Pe indicates that the advective transport dominates over diffusion. The value of $Da \ll 1$ indicates that the reaction rate is slower compared to the advective transport rate.

3. Results and discussion

3.1. Ghost features of dissolution

Fig. 1a shows a three-dimensional image of the original dry scan (5 μm voxel size) of the rock sample before dissolution. Fig. 1b and e show two-dimensional high-resolution images (2 μm voxel size) of the original dry scans acquired at a distance of $\sim 9.5 \text{ mm}$ and $\sim 3.5 \text{ mm}$ from the base (inlet) of the sample respectively. Fig. 1c shows the image after dissolution (at the same location as in Fig. 1b). This image shows that the reactive brine dissolved the rock grains at many locations near grain/pore boundaries. This is indicated by newly formed pore space (darker regions with a gray-scale similar to that of brine in pores in Fig. 1c) that was gray (representing grains) before dissolution (Fig. 1b). After oil injection into the sample, strikingly, the oil (white) does not invade all the newly formed pore space (Fig. 1d). It rather stays at the initial grain boundaries (as in Fig. 1b). The grain marked by 'A' in Fig. 1d appears almost completely dissolved in Fig. 1c, however, the oil did not invade this location. Fig. 1f and g show the presence of similar features near the inlet of the sample scanned at two voxel sizes (2 μm and 5 μm). These observations indicate that grains (that appear to be dissolved) are not really completely dissolved and a skeleton of grains (*ghost features* or *ghost regions*) remains in place after dissolution. The possible reason that these ghost features were not identified in X-ray images after dissolution (before oil injection) is the low X-ray attenuation of the remaining skeleton. This can be linked to the formation of high porosity in the ghost regions, resulting in a gray scale (or X-ray attenuation) similar to that of brine in the pore space. At many other locations, we also observe partially dissolved grain boundaries with intermediate gray scale (darker rings around grains in Fig. 1c and d), which are expected to have intermediate porosity values (larger than the porosity of the original grains). We hypothesize that the pore size in the ghost regions (that are water-wet) remain too small for oil (as a non-wetting fluid) to invade them under the flow conditions used in this study.

The formation of ghost regions is expected to be controlled by diffusive flow, though the overall flow in the sample is dominated by advection. Ketton grains have interconnected nanometer-scale pore space. The small size of the intra-granular pores implies an initial permeability many orders of magnitude smaller than that of the macro-pores precluding significant advection, however they can allow the reactive fluid to diffuse and dissolve the intra-grain regions. The effect of diffusion-controlled dissolution is expected to reduce with increasing distance from the surface of the grains.

To explain this further, we use the diffusive Damköhler number (Gervais and Jensen, 2006):

$$Da_{Diff} = kL/D \quad (8)$$

where k is the reaction rate constant, L is the characteristic length which is approximately taken as the radius of a micro-pore $\sim 10^{-7} \text{ m}$, and D is the molecular diffusion coefficient.

For H^+ , $k_1 = 2.5 \times 10^{-4} \text{ m/s}$. Using the H^+ and Cl^- ion pair diffusion coefficient ($D = 5.6 \times 10^{-9} \text{ m}^2/\text{s}$), the calculated value of Da_{Diff} is ~ 4.5 , indicating that the protons are likely to be consumed within a few micro-pore radii. However, for the dissolved CO_2 , $k_2 = 5.5 \times 10^{-7} \text{ m/s}$, and the molecular diffusion coefficient of CO_2 in water $D \sim 3.6 \times 10^{-9} \text{ m}^2/\text{s}$ at $\sim 50^\circ \text{C}$ (Cadogan et al., 2014), the calculated value of Da_{Diff} is $\sim 1.5 \times 10^{-5}$. If we consider the average width of the ghost region as $L \sim 6.5 \times 10^{-5} \text{ m}$ (this is discussed in the forthcoming sections), the value of Da_{Diff} is $\sim 9.9 \times 10^{-3}$. This value is still small, indicating that the reaction rates are slow compared to the rate of diffusion and that reaction with the dissolved CO_2 can take place over the width of the ghost regions.

We expect to observe a similar behavior of dissolution and formation of partially dissolved regions after reactive flow in a water-wet rock sample. Previous studies on wettability-altered carbonate minerals (treated similarly to that in the current study) show that the effects of wettability alteration on reaction rates are negligible at the experimental conditions

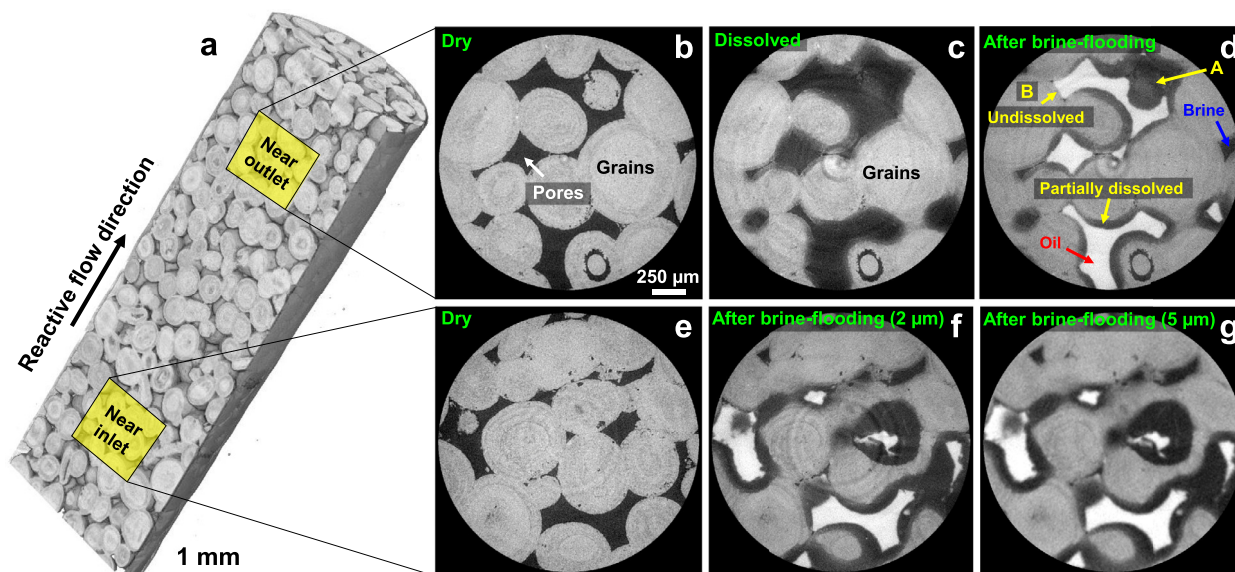


Fig. 1. Dissolution and oil-brine injection. (a) Three-dimensional visualization of the rock sample (at a voxel size of $5\ \mu\text{m}$) before fluid invasion (dry scan), with a clipping plane in the middle along the z-axis. The total height of the final imaged sample, after cropping to remove distorted regions, is $\sim 10.3\ \text{mm}$, the center of which is at $\sim 6.54\ \text{mm}$ from the base (inlet) of the $13.3\ \text{mm}$ long rock sample. (b) A high-resolution two-dimensional horizontal cross-section of the original dry scan at a voxel size of $2\ \mu\text{m}$ acquired near the top (outlet) at a distance of $\sim 9.5\ \text{mm}$ from the base (inlet) of the sample. (c–d) The same image location after dissolution (c) and at the end of sequential oil and brine injection (d). (e) A high-resolution two-dimensional horizontal cross-section of the original dry scans at a voxel size of $2\ \mu\text{m}$, acquired near the inlet at a distance of $\sim 3.5\ \text{mm}$ from the base of the sample. (f–g) The same image location after dissolution and at the end of sequential oil and brine injection at a voxel size of $2\ \mu\text{m}$ (f) and $5\ \mu\text{m}$ (g).

investigated (Anabaraonye, 2017). The partially dissolved features in a water-wet sample can partly be seen in images from previous studies (e.g., Qajar and Arns, 2016), however they were not commented on at the time. Further, we expect that the injection of an oil phase after reactive flow (similar to the procedure used in the present study) can make the identification of these partially dissolved regions unambiguous.

It should be noted that, at many grain boundaries, we do not observe ghost regions or any other indication of alteration, which suggests that the reactive fluid did not dissolve the rock surface, e.g., in Fig. 1d (marked by ‘B’). To confirm that the absence of ghost features occurs at unreacted grain surfaces, we conducted a drainage-imbibition (oil and brine injection) experiment on a separate rock sample without dissolution. Fig. S6 (Supplementary Information) shows that the oil stays in the vicinity of the unreacted grain surfaces without having ghost regions, which is similar to that observed in Fig. 1d (e.g., marked by ‘B’).

Overall, the identification of the ghost features after dissolution provides new insights into the dissolution behavior of a carbonate rock that has intra-granular micro-porosity. Without considering these ghost features, there will be a large uncertainty in the estimation of rock and pore properties. Over-segmentation of the pore space (by considering these ghost features as the bulk pore space, e.g., in Fig. 1c) could result in the incorrect estimation of porosity and flow properties, such as absolute and relative permeability predicted from direct simulations performed on the segmented X-ray micro-tomographic images (Qajar and Arns, 2017; Liu and Mostaghimi, 2018; Pereira Nunes et al., 2016). The uncertainty in segmentation and computed properties can further increase for lower resolution images, e.g. Fig. 1g that was acquired at a voxel size of $5\ \mu\text{m}$. For a comparison of the quality of segmentation for different resolution images, readers are referred to Singh et al. (2016).

3.2. Nano-scale imaging of ghost features

To investigate the ghost features, we conducted nano-scale imaging using FIB-SEM. Fig. 2a shows a three-dimensional image of the resin-filled, cut and polished rock sample that was used for FIB-SEM analysis.

We selected two locations in this study. A1 was selected as a control location where the rock grain did not go through dissolution during reactive fluid injection. This was also confirmed from the tomographic images acquired at the end of sequential oil and brine injection (Figure S7, Supplementary Information). The second location A2 was selected where there were clearly visible ghost regions (dark gray) (also see Fig. S7, Supplementary Information). Fig. 2b, c, e and f show the zoomed-in sections at these selected locations. Fig. 2d and g show the images of trenches at these locations.

Fig. 2h and i show two-dimensional FIB-SEM images acquired at the control location A1 and the partially dissolved location A2 respectively. Fig. 2j and k show the same images after segmentation. We observe a significant increase in the pore space after dissolution. The segmented three-dimensional images of rock and pore spaces are shown in Fig. 3. Fig. 3a and b show the segmented rock and pore space at the location A1 respectively. The different colors in Fig. 3b indicate disconnected clusters of the pore space. The pores that appear disconnected are either due to their presence at the border of the image or due to low image resolution (voxel size of $14.1 \times 17.7 \times 25.4\ \text{nm}$) that did not capture the connectivity of the pore space at the sub-nano scale. The overall porosity of the sample at location A1 is $\sim 6 \pm 2\%$ (mean \pm SD). Fig. 3c shows the porosity profiles in each direction (orientation is indicated in Fig. 2). We do not observe major variations in porosity in the Y and Z directions, which indicates that the porosity along the grain periphery is similar (Fig. 2c). The porosity changes significantly along the X direction (going toward the bulk pore space). The variation in porosity across a grain (along the X direction in Fig. 2c) is expected for the Ketton rock. The Ketton rock is an Oolite, and is composed of nearly spherical grains with concentric layers of different densities and porosities. This observation is consistent with the gray-scale variations across the grain observed in X-ray tomographic images (Fig. 1). The darker concentric layers are more porous (these layers absorb less X-rays due to lower rock density).

Fig. 3 also shows the rock structure (Fig. 3d), the pore space (Fig. 3e) and the porosity profiles in each direction (Fig. 3f) after dissolution at

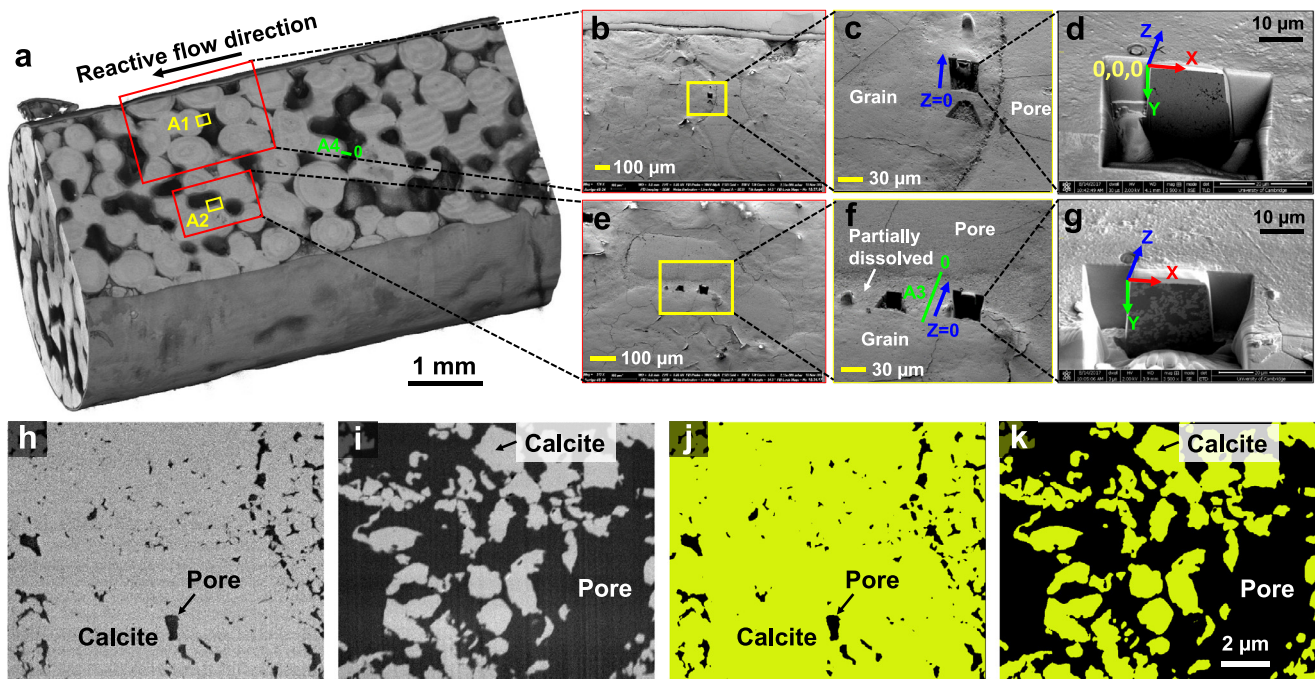


Fig. 2. FIB-SEM imaging. (a) Three-dimensional visualization of the epoxy impregnated and polished sample after dissolution (at a voxel size of $4.65\ \mu\text{m}$). The right hand side is the inlet of the sample where the reactive fluid was injected. The yellow boxes indicate the selected locations for FIB-SEM analysis, where the grains were undissolved (location A1) and partially dissolved (location A2) after reactive flow. (b)–(g) show zoomed-in sections of the locations selected for FIB-SEM. The blue arrows in (c, d, f and g) indicate the direction of milling during FIB-SEM imaging, starting at $Z=0$. Longer trenches of ~ 44 – $66\ \mu\text{m}$ length were excavated at locations A3 and A4 (marked by the green line in (f) and (a) respectively) to image larger sections of partially dissolved grains using SEM. (h–i) Two dimensional cross-sections of the FIB-SEM image acquired at the control location A1 (h) and partially dissolved location A2 (i). Here, black and gray represent pore and rock respectively. (j) and (k) show the same images after segmentation. Here, black and yellow represent binary pore and rock phases respectively. (For interpretation of the references to colour in this figure legend, the reader is referred to the web version of this article.)

location A2. The porosity is almost constant only along the Y direction. Along the Z direction (toward the bulk pore space—Fig. 2f), the porosity increases from approximately 45% to 65–80%. This is expected as the diffusion-controlled dissolution effects are more predominant near the bulk pore space where the reactive fluid flows adjacent to grain boundaries. The overall porosity of partially dissolved regions at location A2 is $64 \pm 5\%$, which is an order of magnitude larger than that at the control location A1. This substantial difference in porosity indicates that the reactive fluid has accessed the nano-scale pore space and dissolved the rock significantly.

The pore size distribution also shows significant differences at the control and partially-dissolved locations (Fig. 3). At the control location, the pore size ranges from $34\ \text{nm}$ to $307\ \text{nm}$ with a clear peak at $77\ \text{nm}$ (Fig. 3g). On the other hand, we observe up to an order of magnitude increase in the pore sizes of the ghost regions. The ghost regions show a wide spread in the distribution (Fig. 3h), with pore sizes in the range $54\ \text{nm}$ to $1.1\ \mu\text{m}$, with a peak at $390\ \text{nm}$ (Fig. 3h).

3.3. Characterization of the thickness of ghost regions after dissolution

Due to limited resources, the three-dimensional FIB-SEM could only cover a region of ~ 10 to $\sim 18\ \mu\text{m}$ in size. For investigating the overall view of partially dissolved regions across a grain, we excavated two longer trenches of ~ 44 to $\sim 66\ \mu\text{m}$ length. Two-dimensional SEM images were then acquired at these locations. The location A3 was selected at approximately $43\ \mu\text{m}$ from the partially dissolved location A2 along the X direction (refer to Fig. 2f). The scanned image, along with its segmented image and porosity profile, is shown in Fig. 4 (a, b and e). The calculated porosity varies from 100% (in the bulk pore space) to approximately 0–8% in the grain (which is unreacted). The value of 0–8% porosity in the undissolved grain is in agreement with the values ob-

tained from the FIB-SEM volume of the control location A1 ($\sim 6\%$). The partially dissolved location A2 (Fig. 3d–f) was imaged at an approximate distance of $25\ \mu\text{m}$ from the bulk pore space (refer to Fig. 2f). The porosity profile at A2 along the Z axis (Fig. 3f) is in close agreement to the plot (blue) in Fig. 4e between $\sim 25\ \mu\text{m}$ and $\sim 35\ \mu\text{m}$. Small variations are expected as we have observed in Fig. 3f, in which the porosity along the X direction varies significantly over a short distance.

Fig. 4c and d show the SEM image of the second longer trench at the location A4 (marked in Fig. 2a), which was selected at a distance of $\sim 1.9\ \text{mm}$ from the location A3, toward the inlet of the sample. The porosity values of the partially dissolved regions at location A4 are in the same range as that of A3 (compare black and blue in Fig. 4e). The only difference we observe is that the width of the partially dissolved region is significantly larger than at location A3.

To investigate the difference in the width of partially dissolved regions with a wider field of view, we also measured the thickness of these regions from two high-resolution tomographic images (Fig. 1d and f) obtained after sequential oil and brine flooding near the outlet and the inlet of the sample. The thickness between oil (representing the bulk pore space without any partially dissolved grains) and the undissolved grain surfaces (refer to the inset picture of Fig. 5 and Fig. S4 in Supplementary Information) was measured manually at more than 400 locations for each tomographic image. Fig. 5 shows the histograms of the thickness measured near the inlet and the outlet of the sample. The average thickness of partially dissolved regions near the inlet and the outlet of the sample is $75 \pm 33\ \mu\text{m}$ (mean \pm SD) and $55 \pm 22\ \mu\text{m}$ respectively. This is consistent with the width of partially dissolved regions at location A3 and A4, shown in Fig. 4. Location A3 is closer to the outlet of the sample where dissolution effects are less compared to A4 toward the inlet.

Near the inlet, we also observe completely dissolved grain surfaces that did not have ghost features. This is shown in Fig. S8 (Supple-

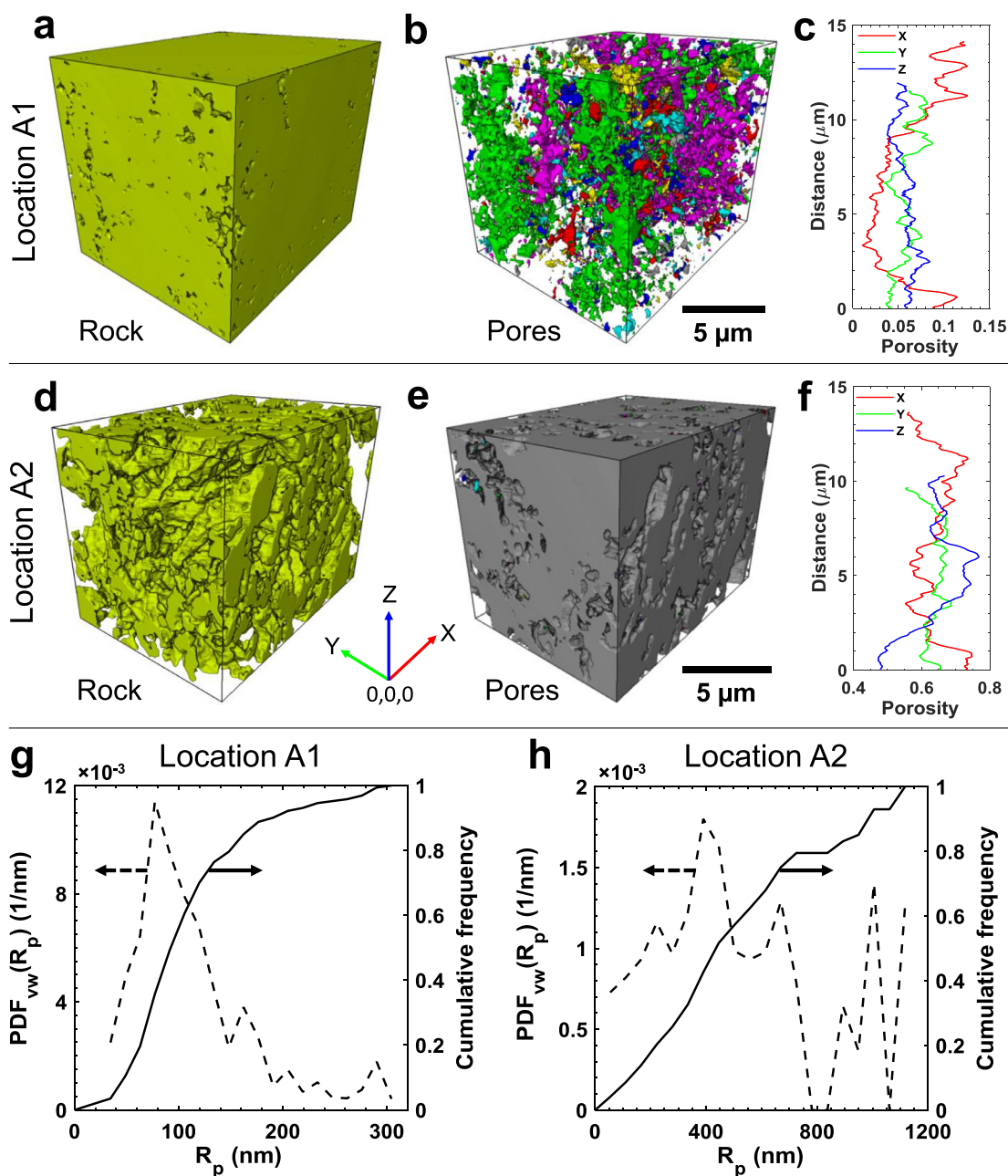


Fig. 3. Three-dimensional nano-scale imaging and pore characterization. (a and b) Three-dimensional FIB-SEM images showing rock (a) and pore space (b) of the control location A1. The different colors in (b) represent disconnected clusters of the pore space. This is either due to their presence at the border of the image or due to image resolution (voxel size of $14.1 \times 17.7 \times 25.4$ nm) which did not allow us to detect their connectivity. (c) Porosity profiles at the control location A1 in X, Y and Z directions. (d and e) Three-dimensional FIB-SEM images (voxel size of $13.7 \times 17.1 \times 25.2$ nm) showing rock (d) and pore space (e) of the partially dissolved location A2. The pore space was completely connected (represented by a single shade of gray in (e)), except for a few small disconnected pores at the boundaries of the image (shown in different colors) (f) Porosity profiles at the location A2 in X, Y and Z directions. (g–h) PDF and cumulative frequency of the pore size distributions of the control sample location A1 (g) and partially dissolved sample location A2 (h). Here, the dashed arrows indicate the data (shown in dashed lines) to their respectively-axis, i.e., left axis for PDF. The solid arrows indicate the data (shown in solid lines) to their respective y-axis, i.e., right axis for cumulative frequency.

mentary Information), in which ‘A’ indicates the location where the rock did not form ghost regions after dissolution. We speculate that at these locations, a complete dissolution of grains occurs due to unconnected intra-grain micro-porosity, which does not allow diffusion of the reactive fluid into the grains, therefore limiting the formation of ghost regions, or represent areas where all the rock had dissolved completely.

3.4. Overall dissolution behavior along the height of the sample

Fig. 6 shows the porosity profile of the rock (dry scan) before dissolution (black). The porosity is uniform along the height of the sample. The overall porosity of the sample before dissolution is $15 \pm 2\%$ (mean \pm SD). The porosity increased by approximately a factor of two after dissolution. The overall porosity after dissolution ranges from $27 \pm 6\%$ to

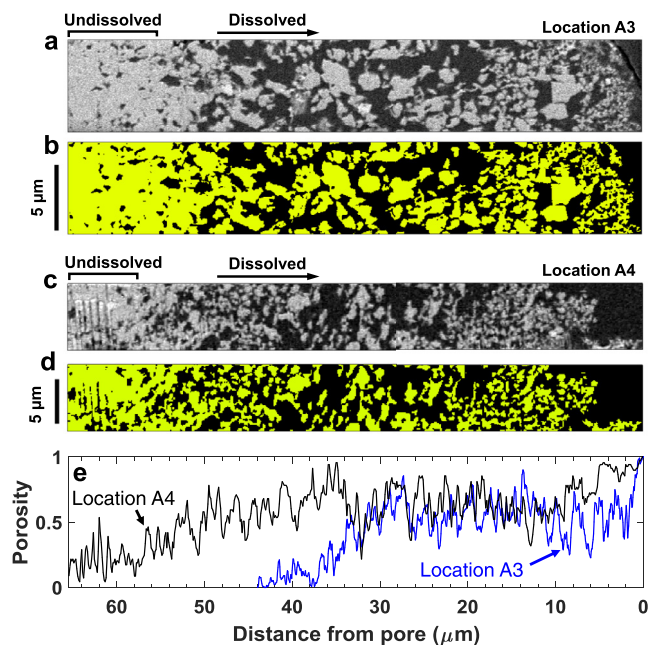


Fig. 4. SEM images across partially dissolved regions at location A3 (near location A2) and location A4. (a and b) Two-dimensional SEM images showing the original gray-scale (a) and segmented (b) image of the longer trench at location A3, which was cut near the location A2. The orientation and the starting point (0) are marked on Fig. 2f. A pixel size of 53.9 nm was used. (c and d) Two-dimensional SEM images showing the original gray-scale (c) and segmented (d) image of the longer trench that was excavated at location A4 (see Fig. 2a). The pixel size is 111.5 nm. The right hand side of images (a-d) is toward the bulk pore space of the sample and the left hand side is the undissolved grain. (e) Porosity profiles obtained from segmented images. The porosity profiles of the location A3 and location A4 are shown in blue and black respectively.

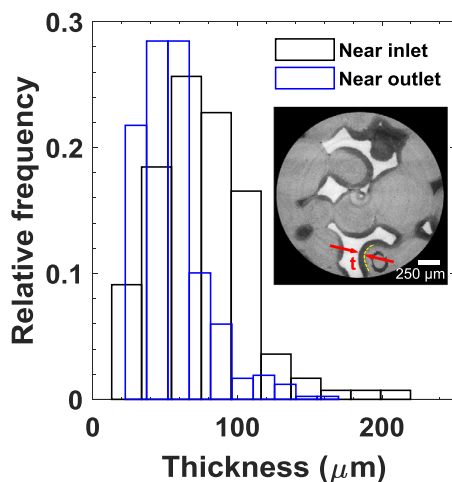


Fig. 5. Thickness of partially dissolved regions. The histograms show the measurements of the thickness of partially dissolved regions at two different locations near the inlet and outlet of the sample. The analysis was conducted on more than 400 points on the high resolution tomographic images shown in Fig. 1d and f. The overall thickness profiles near the inlet is slightly larger than that at the top of the sample, indicating more diffusion-controlled dissolution. The inset picture shows an example location of thickness measurement 't' near the outlet of the sample. The details are provided in Fig. S4 (Supplementary Information).

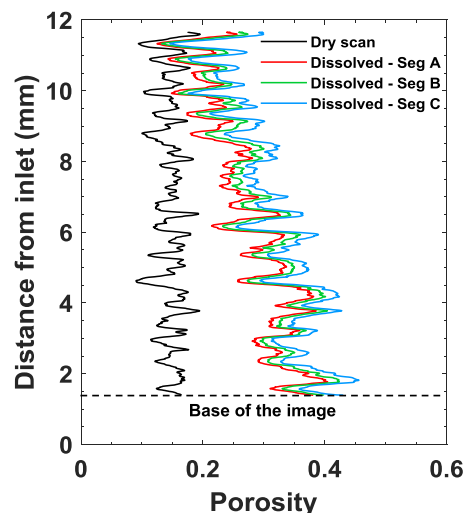


Fig. 6. Overall dissolution behavior. The porosity profiles of the rock before dissolution and after injecting supercritical CO_2 -saturated reactive brine. Three plots for the dissolved sample (Seg A, Seg B and Seg C) correspond to different segmentation thresholds as explained in Figure S2 (Supplementary Information). The base of the processed and cropped image is at ~ 1.39 mm from the base of the rock sample (see Fig. 1 for details).

$31 \pm 6\%$ for different segmentation thresholds (see Figure S2, Supplementary Information). Although we observe a variation in the porosity distributions for different segmentation thresholds, the overall trend of all three plots is the same (red, green and blue in Fig. 6). We observe a uniform dissolution up to 4 mm from the inlet of the sample. Thereafter, the amount of dissolution decreases with distance from the injection point, as the system potentially approaches equilibrium near the outlet (top) of the sample. This observation is also consistent with the thickness profiles of partially dissolved (ghost) regions near the inlet and outlet. The thickness decreases with increasing distance from the injection point, indicating a decreasing amount of diffusion-controlled dissolution in micro-pores (Fig. 4 and Fig. 5).

3.5. Permeability and flow fields: evaluation of the effect of segmentation thresholds

The permeability of the rock sample was calculated directly from the segmented pore space using the procedure described in Section 2.3.5. The permeability of the dry scan (before dissolution) is found to be $3.2 \times 10^{-12} \text{ m}^2$, which increased significantly after dissolution, however the extent of this increase is dependent on the segmentation threshold. The values of permeability for Seg A, Seg B and Seg C are found to be $6 \times 10^{-11} \text{ m}^2$, $8.8 \times 10^{-11} \text{ m}^2$ and $1.10 \times 10^{-10} \text{ m}^2$ respectively. The permeability values vary approximately by a factor of two, depending of which portion of the partially dissolved rock is segmented as pore space (in Seg A, Seg B and Seg C). Fig. 7a shows a three-dimensional image of the velocity fields in the pore space of the segmented dry scan, and Fig. 7b–d show the velocity fields in the pore space after dissolution for various segmentation thresholds (Seg A, Seg B and Seg C). Fig. 7e–h show the corresponding two-dimensional horizontal cross-sections through the middle of the sample. As the pore space increases (with different segmented thresholds from Seg A to Seg C), the pore-scale velocity reduces at many locations (e.g. location 'x' in Fig. 7g and h). We also observe the formation of a focused flow field with high pore-scale velocities as the segmented pore space expands from Seg A to Seg B (location 'y' in Fig. 7g). These observations demonstrate that the flow fields and permeability are sensitive to how the pore space is segmented. We suspect that the changes in segmented pore space can significantly affect the relative permeability in the case of two-phase flow simulations;

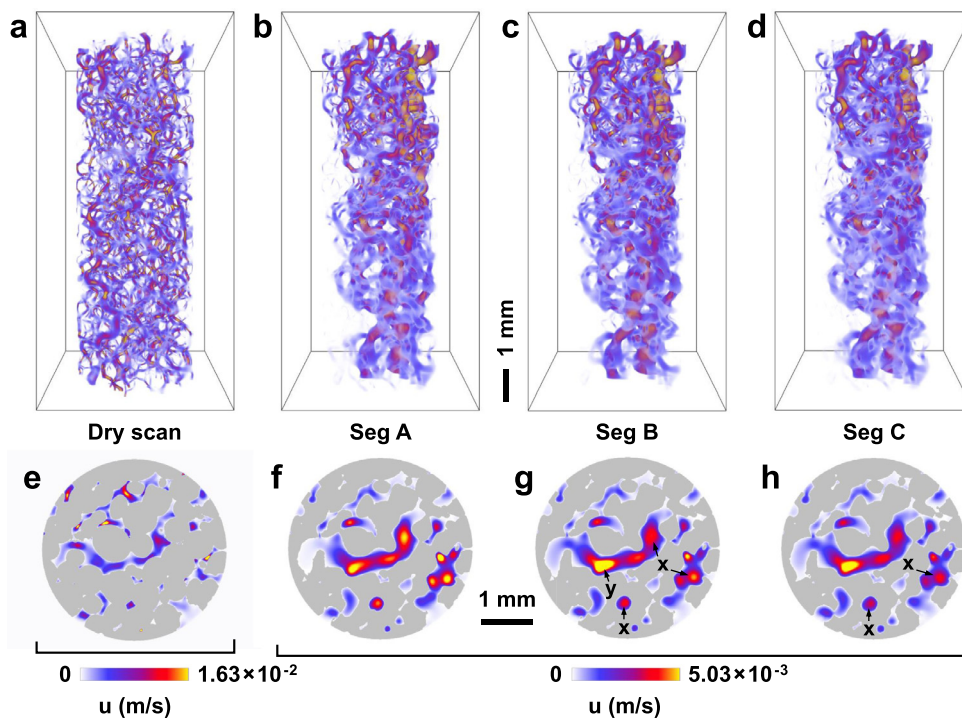


Fig. 7. Velocity fields before and after dissolution. (a) Flow field simulations using the Navier-Stokes equation on the segmented pore space of the dry scan. (b–d) Flow field simulations on the pore space after dissolution for Seg A (b), Seg B (c) and Seg C (d). (e–f) show the corresponding two-dimensional horizontal cross-sections through the middle of the sample, indicating flow fields in the segmented pore space for dry scan (e), Seg A (f), Seg B (g) and Seg C (h).

however, these simulations are out of the scope of the current study. We also note that the Ketton limestone used in this study has a very well connected and open macro pore space and much larger differences may be obtained in lower permeability samples.

Future studies can also focus on the evaluation of the experimental permeability of rock samples after dissolution, which can be achieved by adopting a flow injection strategy of oil injection after dissolution (similar to that presented in the current study). Additionally, a water-wet membrane can be placed at the base of the sample, which can restrict the passage of oil (non-wetting phase) during pressure-controlled oil injection, therefore providing a complete oil saturation in the macro pores of the rock after oil injection. In this way, the effective segmentation of the bulk pore space can be achieved, which can result in the isolation of partially dissolved regions. These partially dissolved regions can then be assigned their own permeability while calculating the overall permeability through the dissolved sample.

4. Conclusions

In this study, we have used X-ray micro-tomography and FIB-SEM to investigate the dissolution behavior of an oil-wet carbonate rock sample after the injection of reactive supercritical CO_2 -saturated brine. The sample was first saturated with a non-reactive brine, followed by injection of a reactive supercritical CO_2 -saturated brine. The reactive brine was replaced with a non-reactive brine, followed by sequential injection of oil and brine. The sample was imaged after each injection step. Furthermore to characterize the dissolution features at the nano-scale, the sample was imaged using a FIB-SEM.

Our findings provide new insights into the dissolution behavior of carbonate rock grains that have intra-grain micro-porosity. The injection of oil after dissolution revealed the presence of partially dissolved (ghost) regions that were difficult to visualize from the X-ray micro-tomographic images obtained after dissolution without the presence of a second, non-wetting, fluid phase. These ghost features are expected to occur in a diffusion-limited regime, although the macro-pores experi-

ence an advection dominated flow regime with high Péclet number and low Damköhler number. We expect to observe a similar behavior of rock dissolution and formation of ghost regions in water-wet rock samples.

We computed various parameters to characterize these ghost regions. The overall porosity (obtained from FIB-SEM) of these ghost regions is $64 \pm 5\%$, which is significantly larger than that of a control location without dissolution ($\sim 6 \pm 2\%$). The pore size increased approximately by an order of magnitude after dissolution. The average thickness of the ghost regions decreased from $75 \mu\text{m}$ near the inlet to $55 \mu\text{m}$ near the outlet of the sample. This finding is consistent with the overall dissolution behavior of the complete sample, in which we observe a decreasing trend of dissolution toward the outlet. In addition, near the inlet, we also observe that the ghost regions did not form in a few grains; rather a complete dissolution of the rock occurred.

We show that these ghost regions have a significant impact on the porosity and permeability. Without considering these ghost features, there will be large uncertainties in predicting the correct values of permeability and relative permeability calculated from simulations on segmented X-ray micro-tomographic images. If it is assumed that the grains dissolve with a sharp reaction front, it is likely that the change in permeability is significantly over-estimated. Although, we have examined these features in a quarry rock sample, a similar behavior is expected in any carbonate rock grains containing intra-granular micro-porosity.

Conflicts of interest

There are no conflicts to declare.

Data availability

The SEM, FIB-SEM and X-ray tomographic datasets used in the current study are available in the British Geological Survey repository (<http://www.bgs.ac.uk/services/ngdc/citedData/catalogue/31a77ab1-8f21-4a10-8540-034da0dece1e.html>) (ref. Singh et al., 2018). Any

additional data that support the findings and analysis are available from the corresponding author upon request.

Acknowledgments

We gratefully acknowledge funding from the Qatar Carbonates and Carbon Storage Research Centre (QCCSRC), provided jointly by Qatar Petroleum, Shell, and Qatar Science & Technology Park. K.S. gratefully acknowledges Tom Bultreys and Takashi Akai for help in imaging and image processing, Richard Langford for FIB-SEM image acquisition, and Ali Raeini for help in performing the flow simulations.

Supplementary materials

Supplementary material associated with this article can be found, in the online version, at doi:10.1016/j.advwatres.2018.09.005.

References

- Al-Khulaifi, Y., et al., 2018. Reservoir-condition pore-scale imaging of dolomite reaction with supercritical CO₂ acidified brine: effect of pore-structure on reaction rate using velocity distribution analysis. *Int. J. Greenhouse Gas Control* 68, 99–111.
- Anabaraonye, B.U., 2017. *Experimental and modelling studies of reservoir mineral dissolution following carbon dioxide injection*, PhD thesis. Imperial College London. Available from: <http://hdl.handle.net/10044/1/61347>.
- Andrew, M., Bijeljic, B., Blunt, M.J., 2014. Pore-scale imaging of trapped supercritical carbon dioxide in sandstones and carbonates. *Int. J. Greenhouse Gas Control* 22, 1–14.
- Arganda-Carreras, I., et al., 2017. Trainable Weka Segmentation: a machine learning tool for microscopy pixel classification. *Bioinformatics* 33 (15), 2424–2426.
- Bachu, S., Gunter, W.D., Perkins, E.H., 1994. Aquifer disposal of CO₂: hydrodynamic and mineral trapping. *Energy Convers. Manage.* 35 (4), 269–279.
- Berg, S., et al., 2013. Real-time 3D imaging of Haines jumps in porous media flow. In: *Proceedings of the National Academy of Sciences*, 110, pp. 3755–3759.
- Bijeljic, B., et al., 2013. Predictions of non-Fickian solute transport in different classes of porous media using direct simulation on pore-scale images. *Phys. Rev. E* 87 (1), 013011.
- Blunt, M.J., et al., 2013. Pore-scale imaging and modelling. *Adv. Water Resour.* 51 (0), 197–216.
- Blunt, M.J., 2017. *Multiphase Flow in Permeable Media: A Pore-Scale Perspective*. Cambridge University Press, Cambridge.
- Boot-Handford, M.E., et al., 2014. Carbon capture and storage update. *Energy Environ. Sci.* 7 (1), 130–189.
- Cadogan, S.P., Maitland, G.C., Trusler, J.P.M., 2014. Diffusion coefficients of CO₂ and N₂ in water at temperatures between 298.15 K and 423.15 K at pressures up to 45 MPa. *J. Chem. Eng. Data* 59 (2), 519–525.
- Cantrell, D.L., Swart, P., Hagerty, R.M., 2004. Genesis and characterization of dolomite, Arab-D reservoir, Ghawar field, Saudi Arabia. *GeoArabia* 9 (2), 11–36.
- Daccord, G., Liétard, O., Lenormand, R., 1993. Chemical dissolution of a porous medium by a reactive fluid—II. convection vs reaction, behavior diagram. *Chem. Eng. Sci.* 48 (1), 179–186.
- Dong, H., Blunt, M.J., 2009. Pore-network extraction from micro-computerized-tomography images. *Phys. Rev. E* 80 (3), 036307.
- El-Maghraby, R.M., et al., 2012. A fast method to equilibrate carbon dioxide with brine at high pressure and elevated temperature including solubility measurements. *J. Supercrit. Fluids* 62, 55–59.
- Gervais, T., Jensen, K.F., 2006. Mass transport and surface reactions in microfluidic systems. *Chem. Eng. Sci.* 61 (4), 1102–1121.
- Hamouda, A.A., Rezaei Gomari, K.A., 2006. Influence of temperature on wettability alteration of carbonate reservoirs. *SPE/DOE Symposium on Improved Oil Recovery*. Society of Petroleum Engineers, Tulsa, Oklahoma, USA.
- Hansen, G., Hamouda, A.A., Denoyel, R., 2000. The effect of pressure on contact angles and wettability in the mica/water/n-decane system and the calcite+stearic acid/water/n-decane system. *Colloids Surf., A*: 172 (1–3), 7–16.
- Herzog, H., Caldeira, K., Reilly, J., 2003. An issue of permanence: assessing the effectiveness of temporary carbon storage. *Clim. Change* 59 (3), 293–310.
- Krevor, S., et al., 2015. Capillary trapping for geologic carbon dioxide storage – from pore scale physics to field scale implications. *Int. J. Greenhouse Gas Control* 40, 221–237.
- Liu, M., Mostaghimi, P., 2018. Numerical simulation of fluid-fluid-solid reactions in porous media. *Int. J. Heat Mass Transfer* 120, 194–201.
- Luquot, L., Gouze, P., 2009. Experimental determination of porosity and permeability changes induced by injection of CO₂ into carbonate rocks. *Chem. Geol.* 265 (1), 148–159.
- Luquot, L., Rodriguez, O., Gouze, P., 2014. Experimental characterization of porosity structure and transport property changes in limestone undergoing different dissolution regimes. *Transp. Porous Media* 101 (3), 507–532.
- Menke, H.P., et al., 2015. Dynamic three-dimensional pore-scale imaging of reaction in a carbonate at reservoir conditions. *Environ. Sci. Technol.* 49 (7), 4407–4414.
- Menke, H.P., et al., 2018. 4D multi-scale imaging of reactive flow in carbonates: assessing the impact of heterogeneity on dissolution regimes using streamlines at multiple length scales. *Chem. Geol.* 481, 27–37.
- Menke, H.P., Bijeljic, B., Blunt, M.J., 2017. Dynamic reservoir-condition microtomography of reactive transport in complex carbonates: effect of initial pore structure and initial brine pH. *Geochim. Cosmochim. Acta* 204, 267–285.
- Muljadi, B.P., et al., 2016. The impact of porous media heterogeneity on non-Darcy flow behaviour from pore-scale simulation. *Adv. Water Resour.* 95 (Supplement C), 329–340.
- Ott, H., et al., 2012. Core-flood experiment for transport of reactive fluids in rocks. *Rev. Sci. Instrum.* 83 (8), 084501.
- Ott, H., Oedai, S., 2015. Wormhole formation and compact dissolution in single- and two-phase CO₂-brine injections. *Geophys. Res. Lett.* 42 (7), 2270–2276.
- Pak, T., et al., 2015. Droplet fragmentation: 3D imaging of a previously unidentified pore-scale process during multiphase flow in porous media. In: *Proceedings of the National Academy of Sciences*, 112, pp. 1947–1952.
- Peng, C., et al., 2015. Kinetics of calcite dissolution in CO₂-saturated water at temperatures between (323 and 373) K and pressures up to 13.8 MPa. *Chem. Geol.* 403, 74–85.
- Pereira Nunes, J.P., Blunt, M.J., Bijeljic, B., 2016. Pore-scale simulation of carbonate dissolution in micro-CT images. *J. Geophys. Res.: Solid Earth* 121 (2), 558–576.
- Qajar, J., Arns, C.H., 2016. Characterization of reactive flow-induced evolution of carbonate rocks using digital core analysis- part 1: assessment of pore-scale mineral dissolution and deposition. *J. Contam. Hydrol.* 192 (Supplement C), 60–86.
- Qajar, J., Arns, C.H., 2017. Characterization of reactive flow-induced evolution of carbonate rocks using digital core analysis - Part 2: calculation of the evolution of percolation and transport properties. *J. Contam. Hydrol.* 204, 11–27.
- Raeini, A.Q., Bijeljic, B., Blunt, M.J., 2017. Generalized network modeling: network extraction as a coarse-scale discretization of the void space of porous media. *Phys. Rev. E* 96 (1), 013312.
- Shah, S.M., Crawshaw, J.P., Boek, E.S., 2014. Preparation of microporous rock samples for confocal laser scanning microscopy. *Pet. Geosci.* 20 (4), 369–374.
- Singh, K., et al., 2017b. Dynamics of snap-off and pore-filling events during two-phase fluid flow in permeable media. *Sci. Rep.* 7 (1), 5192.
- Singh, K., et al., 2017a. The role of local instabilities in fluid invasion into permeable media. *Sci. Rep.* 7 (1), 444.
- Singh, K., et al., 2018. FIB-SEM and X-ray Micro-Tomographic Images of Carbonate Rock Dissolution During Reactive CO₂-saturated Brine Injection Under Reservoir Conditions. *British Geological Survey* <http://dx.doi.org/10.5285/31a77ab1-8f21-4a10-8540-034da0dece1e>.
- Singh, K., Bijeljic, B., Blunt, M.J., 2016. Imaging of oil layers, curvature and contact angle in a mixed-wet and a water-wet carbonate rock. *Water Resour. Res.* 52 (3), 1716–1728.
- Tanino, Y., Blunt, M.J., 2012. Capillary trapping in sandstones and carbonates: dependence on pore structure. *Water Resour. Res.* 48 (8), 1–13.
- Xu, T., Apps, J.A., Pruess, K., 2003. Reactive geochemical transport simulation to study mineral trapping for CO₂ disposal in deep arenaceous formations. *J. Geophys. Res.: Solid Earth* 108 (B2).